Conference on Modelling Fluid Flow (CMFF'22)
The 18th International Conference on Fluid Flow Technologies
Budapest, Hungary, August 30-September 2, 2022

State of Art and Challenges in Computational Aeroacoustics

Manfred KALTENBACHER[1], Stefan SCHODER[1], Clemens FREIDHAGER[1]

[1] Institute of Fundamentals and Theory in Electrical Engineering , Graz University of Technology (TU Graz). Inffeldgasse 18, 8010 Graz, Austria. E-mail: manfred.kaltenbacher@tugraz.at

ABSTRACT

Aeroacoustics is a young physical and engineering discipline and a topic of strong ongoing research. Basically, all physical phenomena of flow induced sound are described by the set of compressible flow equations. To achieve a deeper physical understanding of the sound generation phenomena, the sound propagation and its interaction, physical models and appropriate numerical simulation schemes are needed. In doing so, the physics of the famous inhomogeneous wave equation of Lighthill and its extensions, as well as perturbation equations based on systematic decomposition of physical field properties are discussed. Furthermore, three different benchmark cases are presented, which serve as important building blocks for the development of new physical models and numerical simulation schemes.

Keywords: Aeroacoustics, analogies, perturbation equations, Helmholtz decomposition

NOMENCLATURE

c	[m/s]	speed of sound
H	[m^2 / s^2]	total enthalpy
$\underline{L}$	[m/s^2]	Lamb vector
l_{ch}	[m]	characteristic length scale
Ma	[-]	Mach number
$\underline{n}$	[-]	unit normal vector
p	[Pa]	total pressure
$\overline{p}$	[Pa]	time mean pressure
p'	[Pa]	fluctuating pressure
p^{a}	[Pa]	acoustic pressure
p^{ic}	[Pa]	incompressible pressure
$\underline{\underline{T}}$	[Pa]	Lighthill tensor
u_{ch}	[m/s]	characteristic flow velocity
$\underline{u}$	$[m/s]$	total velocity vector
$\overline{\underline{u}}$	$[m/s]$	time mean velocity vector
$\underline{u}^{\mathrm{a}}$	$[m/s]$	acoustic particle velocity vector
$\underline{u}^{\mathrm{ic}}$	$[m/s]$	incompressible velocity vector
$\underline{x}$	[m]	observer coordinate vector
$\underline{y}$	[m]	source coordinate vector
δ	[-]	Kronecker delta
λ	[m]	wavelength
ρ	[kg/m^3]	total density
ρ'	[kg/m^3]	fluctuating density
ρ^{a}	[kg/m^3]	acoustic density
$\underline{\underline{\tau}}$	[N/m^2]	viscous stress tensor
φ	[m^2/s]	scalar flow potential
ψ	[m^2/s]	scalar acoustic potential
$\underline{\omega}$	[1/s]	vorticity vector

Subscripts and Superscripts

a	acoustic
c	compressible
ch	characteristic
ic	incompressible
ref	reference
-	temporal mean
0	constant physical value

1. INTRODUCTION

The sound generated by a flow in an unbounded fluid is usually called *aerodynamic sound*. Most unsteady flows in technical applications are of high Reynolds number, and the acoustic radiation is a very small by-product of the motion. Thereby, turbulence is usually produced by fluid motion over a solid body and/or by flow instabilities.

Since the beginning of computational aeroacoustics (CAA) several physical models and numerical schemes have been developed, each of these trying to overcome the challenges for an effective and accurate computation of the radiated sound. The challenges that have to be considered for the simulation of flow induced sound include [1, 2, 3, 4]:

- *Energy disparity and acoustic inefficiency:* There is a large disparity between the energy in the flow and the radiated acoustic energy. In general, the total radiated power of a turbulent jet scales with $O(u_{\mathrm{ch}}^8/c^5)$ (u_{ch} is the characteristic flow velocity and c the speed of sound), and pressure fluctuations on surfaces inside the flow scales with $O(u_{\mathrm{ch}}^6/c^3)$.

- *Length scale disparity:* Large disparity also occurs between the size of an eddy in the turbulent flow and the wavelength of the generated acoustic sound. Eddies with characteristic length scale l_{ch}, velocity u_{ch}, lifetime l_{ch}/u_{ch}, and frequency f radiate acoustic waves of the same characteristic frequency, but with a much larger length scale being the acoustic wavelength

$$\lambda \propto c\,\frac{l_{\mathrm{ch}}}{u_{\mathrm{ch}}} = \frac{l_{ch}}{\mathrm{Ma}}. \tag{1}$$

  In Eq. (1) Ma denotes the Mach number computed by the ratio of the characteristic velocity u_{ch} over the speed of sound c.

- *Dispersion:* Numerical discretization in space and time converts the original non-dispersive system into a dispersive discretized one. As such, this error has to be kept as small as possible by the numerical schemes, in which both the amplitude and phase of the wave are of crucial importance.

- *Simulation of unbounded domains:* A main issue for the simulation of unbounded domains using volume discretization methods remains the boundary treatment, which needs to be applied to avoid reflections of outgoing vortical structures as well as reflections of waves at the boundary of the computational domain.

In general, aeroacoustic formulations may be categorized as follows: (1) direct numerical simulations resolving all vortical and acoustic scales; (2) aeroacoustic analogies; (3) perturbation equations based on systematic decomposition of physical field properties. In this contribution, the focus is on aeroacoustic analogies and perturbation equations. Direct numerical simulations by solving the full set of compressible flow equations and resolving both vortical and wave components become more and more attractive, due to the increase of computer resources [5, 6, 7, 8]. Still, the application to industrial relevant problems is limited.

2. PHYSICAL MODELING

2.1. Lighthill's analogy and extensions

Lighthill transformed the general equations of mass and momentum conservation to an exact inhomogeneous wave equation whose source terms are important only within the turbulent region [9]. In doing so, the in-homogeneous wave equation was derived

$$\left(\frac{1}{c_0^2}\frac{\partial^2}{\partial t^2} - \frac{\partial^2}{\partial x_i^2}\right) c_0^2(\rho - \rho_0) = \frac{\partial^2 T_{ij}}{\partial x_i \partial x_j}\,. \tag{2}$$

It has to be noted that $(\rho - \rho_0) = \rho'$ is a fluctuating density not being equal to the acoustic density ρ^{a}, but a superposition of flow and acoustic parts within flow regions. Far away form the flow, the fluctuating density ρ' approaches the acoustic density ρ^{a}. Furthermore, the right hand side of (2) contains the *Lighthill stress tensor*, and computes by

$$T_{ij} = \rho u_i u_j + \Big((p - p_0) - c_0^2(\rho - \rho_0)\Big)\delta_{ij} - \tau_{ij}\,. \tag{3}$$

In Eqs. (2) and (3) ρ denotes the total density, ρ_0 the ambient density, c_0 the mean speed of sound, p the total pressure, p_0 the ambient pressure, $\underline{u}$ the total velocity, δ the Kronecker delta and τ_{ij} the components of the viscous stress tensor. In the definition of the Lighthill tensor according to Eq. (3) the term $\rho u_i u_j$ are called the Reynolds stresses. The second term $\Big((p - p_0) - c_0^2(\rho - \rho_0)\Big)\delta_{ij}$ represents the *excess of* moment transfer by the pressure over that in the ideal fluid of density ρ_0 and speed of sound c_0. This is produced by wave amplitude nonlinearity, and by mean density variations in the source flow. The viscous stress tensor τ_{ij} properly accounts for the attenuation of the sound. Please note that the terms in T_{ij} not only account for the generation of sound, but also includes acoustic *self modulation* caused by

- acoustic nonlinearity,
- the convection of sound waves by the flow velocity,
- refraction caused by sound speed variations,
- and attenuation due to thermal and viscous actions.

The influence of acoustic nonlinearity and thermoviscous dissipation is usually sufficiently small to be neglected within the source region. Convection and refraction of sound within the flow region can be important, e.g., in the presence of a mean shear layer (when the Reynolds stress will include terms like $\rho u_{0i} u'_j$, where $\underline{u}_0$ and $\underline{u}'$ respectively denote the mean and fluctuating components of $\underline{u}$). Such effects are described by the presence of unsteady linear terms in T_{ij}. Furthermore, since for practical applications, T_{ij} is obtained by numerically solving the full set of compressible flow equations, the question of how accurate these terms are resolved, is always present.

In summary, Lighthill's inhomogeneous wave equation equipped with appropriate boundary conditions (e.g., sound hard at solid walls) correctly models all physical flow-acoustic effects. However, the whole set of compressible flow dynamics equations has to be solved in order to be able to calculate Lighthill's tensor. This means that both the flow structures and acoustic waves have to be resolved, which is an enormous challenge for any numerical scheme and the computational noise itself may strongly disturb the physical radiating wave components [10]. Therefore, in the theories of Phillips and Lilley interaction effects have been, at least to some extent, moved to the wave operator [11, 12]. These equations predict certain aspects of the sound field surrounding a jet quite accurately, which are not accounted in Lighthill's equation due to the restricted numerical resolution of T_{ij} [13]. Please note that Lighthill was initially interested in solving the problem illustrated in Fig. 1a, of the sound produced by a turbulent nozzle flow. However, at this time a volume discretization by numerical schemes was not feasible and so a transformation of the inhomogeneous wave equation into an integral representation was performed by Green's function of free radiation, resulting in

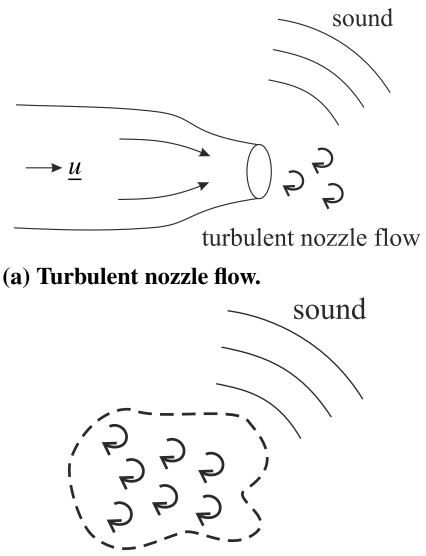

(a) Turbulent nozzle flow.

(b) Isolated turbulent region.

Figure 1. Sound generation by turbulent flows.

$$c_0^2 \rho'(\underline{x}, t) = \frac{1}{4\pi} \frac{\partial^2}{\partial x_i \partial x_j} \int_{-\infty}^{\infty} \frac{T_{ij}(\underline{y}, t - |\underline{x} - \underline{y}|/c_0)}{|\underline{x} - \underline{y}|} \, \mathrm{d}\underline{y} . \tag{4}$$

Thereby, $\underline{y}$ defines the source coordinate and $\underline{x}$ the coordinate at which the acoustic density fluctuation is computed. Therefore, Lighthill's integral formulation just applies to the simple situation as given in Fig. 1b. This avoids complications caused by the presence of the nozzle. Curle investigated the effects of surfaces at rest on the integral solution in terms of Green's function on Lighthill's theory [14]. The extension uses the known facts of distribution theory, and the formulation reads as

$$\begin{aligned} c_0^2 \rho' H(f) \;=\; & \frac{\partial^2}{\partial x_i \partial x_j} \int_{\Omega} \frac{\left\langle T_{ij} \right\rangle}{4\pi |\underline{x} - \underline{y}|} \, \mathrm{d}\underline{y} \\ & - \frac{\partial}{\partial x_i} \oint_{\Gamma_s} \frac{\left\langle (p - p_0)\delta_{ij} - \tau_{ij} \right\rangle}{4\pi |\underline{x} - \underline{y}|} \, \mathrm{d}s_j(\underline{y}) , \end{aligned} \tag{5}$$

where $< \star >$ denotes the evaluation of the term at retarted time and $H(f)$ the Heaviside function of f describing the solid (scatterer) surface Γ_s by

$$f(\underline{x}) = \begin{cases} 0 & \text{for } \underline{x} \text{ on } \Gamma_s \\ < 0 & \text{for } \underline{x} \text{ within the surface} \\ > 0 & \text{for } \underline{x} \text{ in } \Omega \end{cases} . \tag{6}$$

Ffowcs Williams and Hawkings [15] generalized Curle's integral representation towards accounting for the effects of arbitrary moving bodies in the source domain, extending Kirchhoff's formula derived in [16]. The aeroacoustic analogy of Ffowcs Williams and Hawkings[15] is probably one of the most used analogies for free radiation today[17, 18]. However, the integral solution has the restriction that the integration surface must surround all reflection walls and the mean flow field must be constant or zero. The surface may be a physical boundary of a solid or a transparent surface that encloses a fluid body.

For practical applications of Lighthill's analogy, it would be quite beneficial to know the leading order term of Lighthill's tensor. This analysis has been done in [19] for low Mach number flows in an isentropic medium by applying the method of matched asymptotic expansion (see, e.g., [10]). Sound emission from an eddy region involves three length scales: the eddy size l, the wavelength λ of the sound, and a dimension L of the region. The problem is solved for $\mathrm{Ma} \ll 1$ and $L/l \sim 1$ by matching the compressible eddy core scaled by l to a surrounding acoustic field scaled by λ. Thereby, Lighthill's solution is shown to be adequate in both regions, if T_{ij} is approximated by

$$T_{ij} \approx \rho_0 u_i^{\mathrm{ic}} u_j^{\mathrm{ic}} , \tag{7}$$

with $\underline{u}^{\mathrm{ic}} = \nabla \times \underline{\psi}(\underline{\omega})$ and vorticity $\underline{\omega} = \nabla \times \underline{u}^{\mathrm{ic}}$. Such a flow field is described by solving the incompressible flow dynamics equations. Thereby, an incompressible flow velocity $\underline{u}^{\mathrm{ic}}$ and pressure p^{ic} are obtained. For an incompressible flow, the divergence of $\underline{u}^{\mathrm{ic}}$ is zero, which allows to rewrite the second spatial derivative of Eq. (7) by

$$\frac{\partial^2}{\partial x_i x_j} (\rho_0 u_i^{\mathrm{ic}} u_j^{\mathrm{ic}}) = \rho_0 \frac{\partial u_j^{\mathrm{ic}}}{\partial x_i} \frac{\partial u_i^{\mathrm{ic}}}{\partial x_j} . \tag{8}$$

Furthermore, applying the divergence to the conservation of momentum and neglecting viscous stresses provides the following equivalence

$$\frac{\partial^2 p^{\mathrm{ic}}}{\partial x_i^2} = -\rho_0 \frac{\partial^2 u_i^{\mathrm{ic}} u_j^{\mathrm{ic}}}{\partial x_i \partial x_j} . \tag{9}$$

In doing so, the flow is totally separated from the acoustic field, which also means that any influence of the acoustic field on the flow field is neglected. Such an approach belongs to hybrid schemes separating the flow from the acoustic computations [4]. Thereby, an optimal computational grid can be used for each individual physical field achieving highest accuracy. As a result, the two grids may be quite different according to the following criteria: (1)

near walls, the flow grid needs refinement to resolve boundary layers; (2) the flow grid is mostly coarsened towards outflow boundaries to dissipate vortices; (3) the acoustic grid has to transport waves and therefore needs an uniform grid size all over the computational domain. Thereby, any feedback of the acoustic field on the flow field can just be modeled, when the compressible flow equations are solved to resolve all vertical and wave structures.

2.2. Perturbation equations

The acoustic/viscous splitting technique for the prediction of flow induced sound was first introduced in [20], and afterwards many groups presented alternative and improved formulations for linear and nonlinear wave propagation [21, 22, 23, 24]. These formulations are all based on the idea, that the flow field quantities are split into compressible and incompressible parts.

For the following derivation, a generic splitting of physical quantities is applied to the conservation equations

$$p = \bar{p} + p^{\mathrm{ic}} + p^{\mathrm{c}} = \bar{p} + p^{\mathrm{ic}} + p^{\mathrm{a}} \tag{10}$$

$$\underline{u} = \underline{\bar{u}} + \underline{u}^{\mathrm{ic}} + \underline{u}^{\mathrm{c}} = \underline{\bar{u}} + \underline{u}^{\mathrm{ic}} + \underline{u}^{\mathrm{a}} \tag{11}$$

$$\rho = \rho_0 + \rho_1 + \rho^{\mathrm{a}}\,. \tag{12}$$

Thereby the field variables are split into mean and fluctuating parts just like in the LEE (Linearized Euler Equations). In addition the fluctuating field variables are split into acoustic and non-acoustic components. Finally, the density correction ρ_1 is build in as introduced above. This choice is motivated by the following assumptions

- The acoustic field is a fluctuating field.
- The acoustic field is irrotational, i.e. $\nabla \times \underline{u}^{\mathrm{a}} = 0$.
- The acoustic field requires compressible media and an incompressible pressure fluctuation is not equivalent to an acoustic pressure fluctuation.

By doing so, the perturbation equations[1] assuming an incompressible flow are derived

$$\frac{\partial p^{\mathrm{a}}}{\partial t} + \underline{\bar{u}} \cdot \nabla p^{\mathrm{a}} + \rho_0 c_0^2 \nabla \cdot \underline{u}^{\mathrm{a}} = -\frac{\partial p^{\mathrm{ic}}}{\partial t} - \underline{\bar{u}} \cdot \nabla p^{\mathrm{ic}} \tag{13}$$

$$\rho_0 \frac{\partial \underline{u}^{\mathrm{a}}}{\partial t} + \rho_0 \nabla (\underline{\bar{u}} \cdot \underline{u}^{\mathrm{a}}) + \nabla p^{\mathrm{a}} = 0 \tag{14}$$

with spatial constant mean density ρ_0 and speed of sound c_0. This system of partial differential equations is equivalent to the previously published ones [22]. The source term is the substantial derivative of the incompressible flow pressure p^{ic}. Using the acoustic scalar potential ψ^{a} and assuming a spatial constant mean density ρ_0 and speed of sound c_0, Eq. (14) may be rewritten by

$$\nabla \left(\rho_0 \frac{\partial \psi^{\mathrm{a}}}{\partial t} + \rho_0 \, \underline{\bar{u}} \cdot \nabla \psi^{\mathrm{a}} - p^{\mathrm{a}} \right) = 0\,, \tag{15}$$

resulting in

$$p^{\mathrm{a}} = \rho_0 \frac{\partial \psi^{\mathrm{a}}}{\partial t} + \rho_0 \, \underline{\bar{u}} \cdot \nabla \psi^{\mathrm{a}}\,. \tag{16}$$

Now, substituting Eq. (16) into Eq. (13) leads to

$$\frac{1}{c_0^2} \frac{D^2 \psi^{\mathrm{a}}}{Dt^2} - \Delta \psi^{\mathrm{a}} = -\frac{1}{\rho_0 c_0^2} \frac{D p^{\mathrm{ic}}}{Dt}\,; \quad \frac{D}{Dt} = \frac{\partial}{\partial t} + \underline{\bar{u}} \cdot \nabla\,. \tag{17}$$

This convective wave equation fully describes acoustic sources generated by incompressible flow structures and its wave propagation through flowing media. In addition, instead of the original unknowns p^{a} and $\underline{u}^{\mathrm{a}}$ just the scalar unknown ψ^{a} has to be computed. In accordance with the acoustic perturbation equations (APE), this resulting wave equation for the acoustic scalar potential has been named *Perturbed Convective Wave Equation* (PCWE) [26, 27].

Finally, it is of great interest that by neglecting the mean flow $\underline{\bar{u}}$ in Eqs. (13) and (14), one arrives at the linearized conservation equations of acoustics with $\partial p^{\mathrm{ic}} / \partial t$ as a source term

$$\frac{1}{\rho_0 c_0^2} \frac{\partial p^{\mathrm{a}}}{\partial t} + \nabla \cdot \underline{u}^{\mathrm{a}} = \frac{-1}{\rho_0 c_0^2} \frac{\partial p^{\mathrm{ic}}}{\partial t} \tag{18}$$

$$\frac{\partial \underline{u}^{\mathrm{a}}}{\partial t} + \frac{1}{\rho_0} \nabla p^{\mathrm{a}} = 0\,. \tag{19}$$

Again using the scalar potential ψ^{a}, one arrives at

$$\frac{1}{c_0^2} \frac{\partial^2 \psi^{\mathrm{a}}}{\partial t^2} - \nabla \cdot \nabla \psi^{\mathrm{a}} = \frac{-1}{\rho_0 c_0^2} \frac{\partial p^{\mathrm{ic}}}{\partial t}\,. \tag{20}$$

Furthermore, as done in the standard acoustic case, one may apply $\partial / \partial t$ to (18) and $\nabla \cdot$ to (19) and subtract the two resulting equations to arrive at

$$\frac{1}{c_0^2} \frac{\partial^2 p^{\mathrm{a}}}{\partial t^2} - \nabla \cdot \nabla p^{\mathrm{a}} = \frac{-1}{c_0^2} \frac{\partial^2 p^{\mathrm{ic}}}{\partial t^2}\,. \tag{21}$$

Please note, that this equation can also be obtained by starting at Lighthill's inhomogeneous wave equation for incompressible flow, where the second spatial derivative of Lighthill's tensor is substituted by the Laplacian of the incompressible flow pressure (see (9)). Using the decomposition of the fluctuating pressure

$$p' = p^{\mathrm{ic}} + p^{\mathrm{a}}\,,$$

results again into (21). It has to be mentioned that Eq. (21) was originally derived by a different approach in [28], and is known as Ribner's dilatation equation.

[1]For a detailed derivation of perturbation equations both for compressible as well as incompressible flows, see [25]

2.3. Towards general aeroacoustics

A general aeroacoustic formulation composes a hyperbolic left hand side defined by a wave operator $\Box$ and a generic right hand side $RHS(\star)$ [29]

$$\Box p' = RHS(p, \underline{u}, \rho, ...)\,. \tag{22}$$

To this end, Lighthill's inhomogeneous wave equation perfectly fits to this class. It is obvious that the right hand side $RHS(\star)$ of Lighthill's inhomogeneous wave equation contains not only source terms, but also nonlinear and interaction terms between the sound and flow field, which includes effects such as convection and refraction of the sound by the flow (see Sec. 2.1).

In 2003, Goldstein proposed a method to split flow variables $(p, \underline{u}, ...)$ into a base flow (non-radiating) and a remaining component (acoustic, radiating fluctuations) [30]

$$\star = \tilde{\star} + \star'\,. \tag{23}$$

Applying the decomposition to the right hand side of the wave equation (the left hand side of the equation is already treated in this manner during the derivation of the acoustic equation) leads to

$$\Box p' = RHS(\tilde{p}, \underline{\tilde{u}}, \tilde{\rho}, p', \underline{u}', \rho', ...)\,. \tag{24}$$

Now, interaction terms can be moved to the differential operator to take, e.g., convection and refraction effects into account, and even nonlinear interactions can be considered. Therefore, three steps to relax the Mach number constraint imposed by the incompressible flow simulation are proposed:

1. Perform a compressible flow simulation, which incorporates two-way coupling of flow and acoustics.

2. Filtering of the flow field, such that one obtains a pure non-radiating field from which the acoustic sources are computed.

3. Solve with an appropriate wave operator for the radiating field
$$\Box p' = RHS(\tilde{p}, \underline{\tilde{v}}, \tilde{\rho}, ...)\,. \tag{25}$$

Naturally, the incompressibility condition (regarding the concept of a non-radiating base flow of Goldstein) leads to the Helmholtz decomposition of the flow field. An additive splitting on the bounded problem domain Ω of the velocity field $\underline{u} \in \mathrm{L}^2(\Omega)$ in L^2-orthogonal velocity components reads as [31]

$$\underline{u} = \underline{u}^{\mathrm{ic}} + \underline{u}^{\mathrm{c}} + \underline{u}^{\mathrm{h}} = \nabla \times \underline{A}^{\mathrm{ic}} + \nabla \phi^{\mathrm{c}} + \underline{u}^{\mathrm{h}}\,, \tag{26}$$

where $\underline{u}^{\mathrm{ic}}$ represents the solenoidal (non-radiating base flow) part, $\underline{u}^{\mathrm{c}}$ the irrotational (radiating) part and $\underline{u}^{\mathrm{h}}$ the harmonic (divergence-free and curl-free) part of the flow velocity. The scalar potential ϕ^{c} is associated with the compressible part and the property $\nabla \times \underline{u}^{\mathrm{c}} = 0$, whereas the vector potential $\underline{A}^{\mathrm{ic}}$ describes the solenoidal (vortical) part of the velocity field, satisfying $\nabla \cdot \underline{u}^{\mathrm{ic}} = 0$.

Based on the decomposition Eq. (26), the actual computation of the additive velocity components for a bounded domain is formulated, where the total flow field $\underline{u}$ and its derivatives do not decay towards or vanish at the boundaries of the decomposition domain. Thus, one has to include the harmonic part $\underline{u}^{\mathrm{h}}$ of the decomposition, which physically speaking is the potential flow solution of the configuration. Thereby, a domain as depicted in Fig. 2 is considered, with the flow boundaries $\Gamma_{1,...,4}$. Applying the curl to Eq. (26), the vector valued curl-curl equation with the vorticity $\underline{\omega} = \nabla \times \underline{u}$ as forcing is obtained

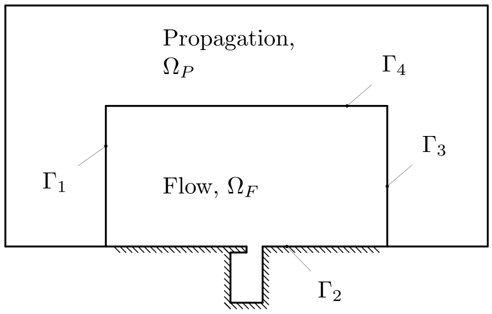

Figure 2. The flow domain Ω_{F} is a subdomain of the acoustic domain Ω_{A}, which includes the flow domain as its source domain and the propagation domain Ω_{P}.

$$\nabla \times \nabla \times \underline{A}^{*,ic} = \nabla \times \underline{u} = \underline{\omega}\,. \tag{27}$$

The star denotes the joint function of both parts, the incompressible and the harmonic one. The function space $\mathcal{W}$ for the vector potential

$$\mathcal{W} = \{\underline{\varphi} \in H(curl, \Omega) | \underline{n} \times \nabla \times \underline{\varphi} = \underline{n} \times \underline{u} \ \text{ on } \Gamma_{1,2,3,4}\}$$

requires a finite element discretization with edge elements (Nédélec elements) [32]. Due to the space $\mathcal{W}$ and the orthogonality condition, the decomposition fulfills along the boundary

$$\int_{\Gamma} \underline{A}^{*,\mathrm{ic}} \cdot (\underline{u}^{\mathrm{c}} \times \underline{n})\mathrm{d}s = 0\,, \tag{28}$$

ensuring the orthogonality of the components and an unique decomposition. Finally, the non-radiating component, which contains all divergence-free components, computes by

$$\underline{\tilde{u}} := \underline{u}^{*,ic} = \nabla \times \underline{A}^{*,ic} = \nabla \times \underline{A}^{ic}\,. \tag{29}$$

For the computation of the wave propagation, the equation of vortex sound [33] based on the total enthalpy

$$H = \int \frac{\mathrm{d}p}{\rho} + \frac{u^2}{2} \tag{30}$$

as primary variable, with $u^2 = \underline{u} \cdot \underline{u}$, is applied. The acoustic analogy for homentropic flow reads as

$$\frac{1}{c^2}\frac{\mathrm{D}^2}{\mathrm{D}t^2} H - \nabla \cdot \nabla H = \nabla \cdot \left(\underline{\omega} \times \underline{\tilde{u}}\right) = \nabla \cdot \underline{L}(\underline{\tilde{u}})\,. \tag{31}$$

The wave operator is of convective type, where the total derivative is defined as

$$\frac{\mathrm{D}\star}{\mathrm{D}t} = \frac{\partial\star}{\partial t} + (\underline{u}\cdot\nabla)\star\ . \tag{32}$$

The aeroacoustic source term is known as the divergence of the Lamb vector $\underline{L}$

$$\underline{L}(\underline{u}) = \left(\underline{\omega}\times\tilde{\underline{u}}\right)\ . \tag{33}$$

3. BENCHMARKS

In the following, three benchmark case are discussed, which are already established or become a standard in the near future to test aeroacoustic formulations.

3.1. Vortex Pair

The rotating vortex pair has been frequently used to determine the capabilities of aeroacoustic methodologies [34, 35, 36]. This arrangement has the nature of a quadrupolar sound field. Figure 3 illustrates the configuration of the vortex pair. Both vortices are delta distributions and oppose each other at a distance of $2r_0$. The strength of each vortex is characterized by the circulation intensity Γ. The vortices rotate around the origin with a period of $T = 8\pi^2 r_0^2/\Gamma$ imposing an angular rotating speed $\underline{\omega}_r = \Gamma/(4\pi r_0^2)\,\underline{e}_3 = \omega_r\,\underline{e}_3$. Each vortex convects the other vortex by a velocity of $\underline{u}_\theta = \Gamma/(4\pi r_0)\,\underline{e}_t$, where $\underline{e}_t$ is the unit vector in tangential direction. The Mach number in the circumferential direction is given by $M_\theta = u_\theta/c = \Gamma/(4\pi r_0 c)$. The potential flow theory can be used to determine the fundamental solution of the spinning vortex pair in terms of the complex flow potential function. In doing so, one introduces the transformation from Cartesian coordinates (x_1, x_2) to the complex plane with the complex coordinate $z = r\exp^{i\theta} = x_1 + ix_2$. The location of each vortex over time t is defined by $b = r_0\exp^{i\omega t}$. Using these definitions, the incompressible, inviscid

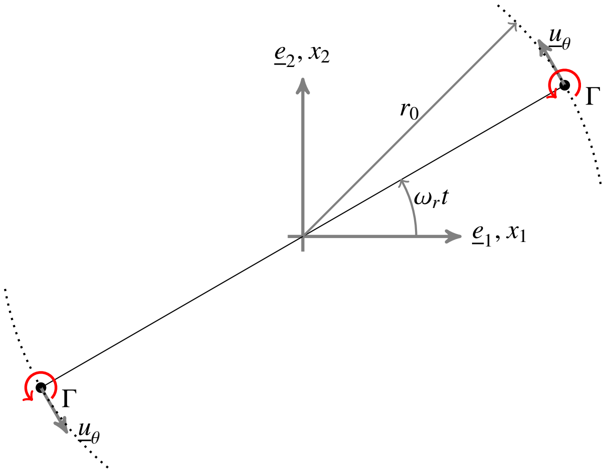

Figure 3. Schematic of the co-rotating vortex pair defining the main geometrical and physical characteristics.

flow potential $\varphi(z,t)$ computes by

$$\varphi(z,t) = \frac{\Gamma}{2\pi i}\ln(z-b) + \frac{\Gamma}{2\pi i}\ln(z+b) = \frac{\Gamma}{2\pi i}\ln(z^2-b^2)\ . \tag{34}$$

The incompressible velocity field $\underline{u}^{ic} = (u_1, u_2)^{\mathrm{T}}$ of the spinning vortex pair is obtained by differentiating Eq. (34) with respect to the complex coordinate z

$$u_1 - iu_2 = \frac{\partial\varphi(z,t)}{\partial z} = \frac{\Gamma}{\pi i}\frac{z}{z^2-b^2}\ . \tag{35}$$

The incompressible fluid dynamic pressure p^{ic} is obtained by applying the unsteady form of Bernoulli's principle

$$p^{\mathrm{ic}} = p_0 - \rho_0\frac{\partial\mathrm{Re}\{\varphi(z,t)\}}{\partial t} - \frac{1}{2}\rho_0(u_1^2+u_2^2)\ . \tag{36}$$

Müller and Obermeier [37] derived an analytic solution of the acoustic far-field, based on matched asymptotic expansion of the potential solution. Starting from the solution in form of a complex potential Eq. (34), matching the inner and the outer solution yields the pressure fluctuation p' of the co-rotating vortex pair

$$p' = \frac{\rho_0\Gamma^4}{64\pi^3 r_0^4 c^2}\Big(J_2(2kr)\cos(2\omega t) - Y_2(2kr)\sin(2\omega t)\Big)\ . \tag{37}$$

In Eq. (37) $k = \omega/c$ denotes the wave number, $J_2(\star)$ the second-order Bessel function of first kind and $Y_2(\star)$ the second kind. It should be emphasized that this fluctuating pressure p' is not equal to the acoustic pressure p^{a}; however, $p' \to p^{\mathrm{a}}$ holds in the far-field.

In doing so, the co-rotating vortex pair on a stationary grid with moving sources induced by the vortical structures are simulated. An unstructured mesh is used to discretize the computational domain. In the source region, a characteristic mesh size of $h \approx 90\,\mathrm{cm}$ is used. Each vortex distribution $\Gamma\delta(z-b)$ is approximated by a continuous multivariant normal distribution with equivalent circulation Γ and an isotropic variance of $\sigma^2 = 0.05\,\mathrm{m}^2$.

The analytic field is represented on the flow grid and is based on a circulation strength of $\Gamma = 2\pi\,\mathrm{m}^2/\mathrm{s}$ and a distance of $2r_0 = 2\,\mathrm{m}$ between the vortices. The angular rotation induced by the vortices is $\omega_r = 0.5\,\mathrm{s}^{-1}$, the speed of sound $c = \sqrt{10}\,\mathrm{m/s}$ and density $\rho_0 = 1\,\mathrm{kg/m}^3$. Using this flow field, the source term computation is performed and finally the sound, which is compared to the analytic solution in the far-field (see Eq. (37)), is computed. The first simulation is based on vortex sound equation according to Eq. (31), and the second computation uses the perturbed convective wave equation (PCWE) as presented in Sec. 2.2. Based on the computational methodology of radial basis functions, the following simulation workflow for the computation of the aeroacoustic source terms is performed. First, the incompressible pressure p^{ic}, flow velocity $\underline{u}^{\mathrm{ic}}$, and vorticity $\underline{\omega}$ are computed. Second, if required, derivatives are computed by the radial basis function framework [38]. As a third step, a conservative interpolation to a much coarser mesh for the acoustic computation is performed [39]. The computational domain of (260 x260) m^2 for the two wave equations is decomposed into three subdomains. The source domain has a diameter of $5r_0$ (relatively high resolved unstructured triangular mesh, $h \approx 90$ cm) is embedded in a propagation region, in which gradually the unstructured mesh size is increased. The propagation region is surrounded by a structured perfectly matched layer (PML) region [40], which absorbs the radiating waves. The wave length $\lambda = \frac{2\pi}{k} \approx 20$ m is resolved (in the propagation region) with approximately 20 linear finite elements per wavelength. For both acoustic simulations, a Newmark scheme with a time step size of $\Delta t = 0.09$ s is applied for the time discretization.

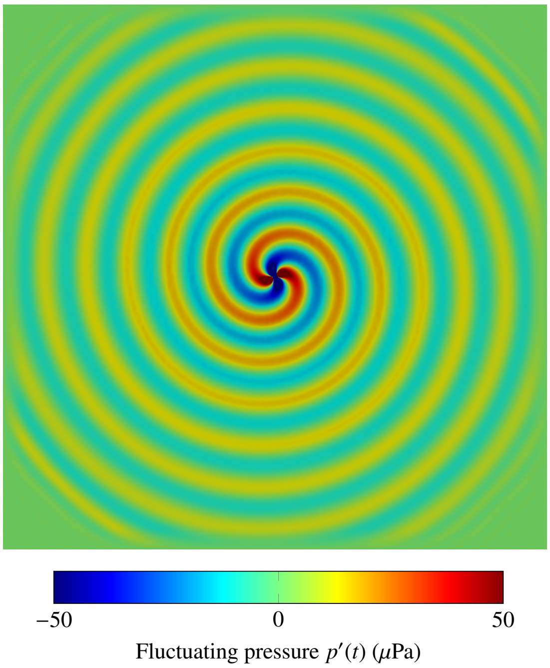

Figure 4. Simulation result solving Eq. (31) **with the Lamb vector as source term.**

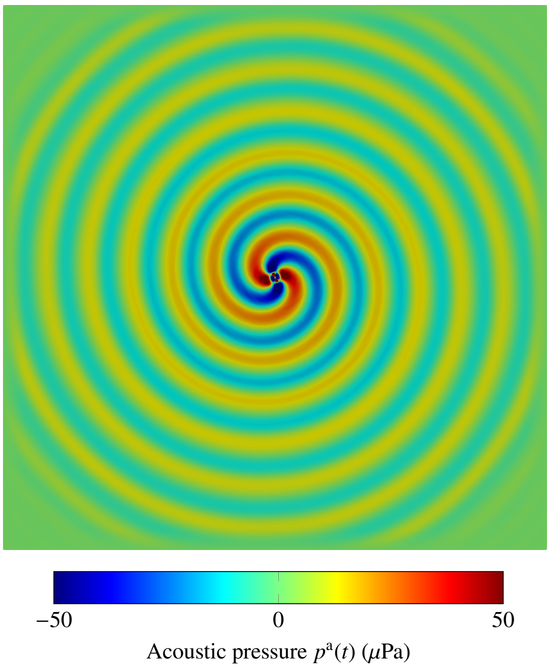

Figure 5. Simulation result solving Eq. (17) **with the substantial derivative of the incompressible pressure as source term.**

Figure 4 shows the fluctuating pressure field of the co-rotating vortex pair obtained by solving Eq. (31). The acoustic field obtained by solving Eq. (17) is displayed in Fig. 5. In the acoustic near-field, differences occur due to the different solution quantities in the two aeroacoustic formulations. Both results have the characteristic radiation pattern of the co-rotating vortex pair.

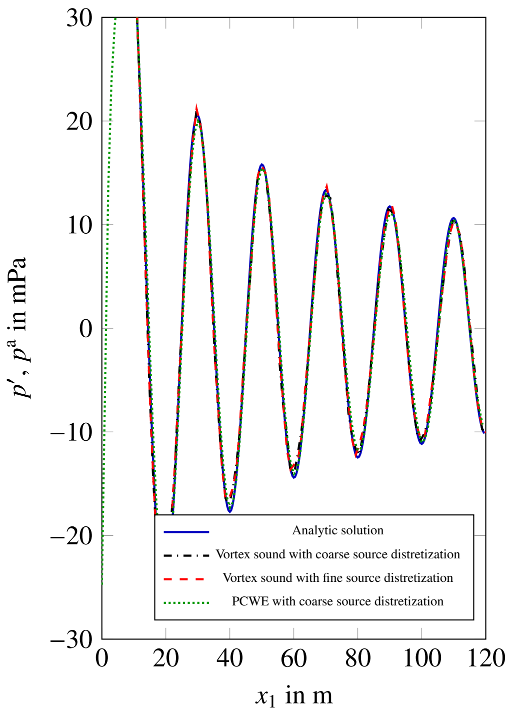

Figure 6. Fluctuating pressure p' and acoustic pressure p^a, respectively, as a function of the coordinate x_1.

The steepest descent of the Gaussian distribution is discretized by 5 linear triangular elements over 2σ. This coarse approximation of the vortical distribution shows the robustness of the radial basis function derivatives. A mesh refinement of the source region (see Fig. 6) causes no significant increase in accuracy compared to the analytic solution. As depicted in Fig. 6, one can clearly see the good accordance of numerical and analytic solution, even for the coarse grid.

3.2. Axial Fan

(a) Axial fan.

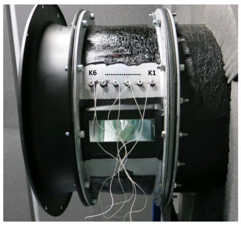

(b) Pressure sensors K1 to K6.

Figure 7. Axial fan and position of the pressure sensors.

The investigated axial fan is displayed in Fig. 7 consisting of nine fan blades with a tip diameter of 495 mm. It was installed inside a duct with a diameter of 500 mm, hence the tip gap was 2.5 mm. The fan was embedded in a sound hard tube and all measurements were performed in a standardized inlet test chamber according to ISO 5801. The test chamber has been built as an anechoic chamber with absorbing walls, ceiling, and floor, to enable aeroacoustic measurements. The rotational speed of the fan was about 1500 rpm, which results in a maximum tip speed of 38.89 m/s. The fan was installed in a short duct with a bellmouth on the in- and outlet to resemble a realistic test setup. The fan was driven by a motor inside the duct. Torque and rotational speed were measured with a precision torque meter. To ensure that torque measurements are not compromised by frictional torque of the bearings, an offset measurement was performed with the fan being removed. All details towards the measurements can be found in [41].

For the numerical computation of the flow field, OpenFOAM Toolbox version 2.3.0 has been used to solve the incompressible Navier-Stokes equations based on the finite-volume method and the arbitrary mesh interface (AMI). The AMI allows simulation across disconnected, but adjacent mesh domains, which are especially required for rotating geometries. The computational domain is displayed in Fig. 8a including the axial fan inside the pipe, the inlet chamber, and the outlet region. The flow solution is computed using an adapted version of the pimpleDyMFoam solver, which can handle dynamic meshes, with a time step size of $\Delta t = 10\,\mu$s. For the CFD computation, a hexahedron-dominant finite volume mesh consisting of 29.8 million cells was generated with the automatic mesh generator HEXPRESSTM / Hybrid from Numeca, as displayed in Fig. 9a. The transient simulation was carried out by using a detached-eddy simulation based on the Spalart-Allmaras turbulence model to accurately resolve the complex flow field. The applied finite-volume scheme has been second order in space and time, and the convective term has been discretized by a bounded central upwind scheme. In total, the CFD computation has been performed for 10 revolutions. After about 6 revolutions, the flow field achieved steady-state and the CFD data of the remaining 4 revolutions have been used for acoustic source and wave propagation computations. Figure 9b displays the flow structure for a characteristic time step.

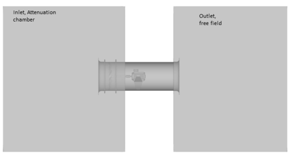

(a) Computational domain for flow computation.

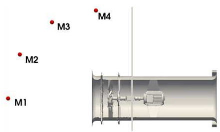

(b) Microphone positions.

Figure 8. Computational domain for flow computation and position of the microphones.

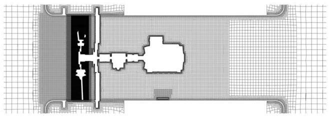

(a) Computational grid.

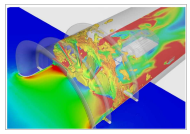

(b) Flow structure.

Figure 9. Cross section through the computational mesh for CFD and flow structure for a characteristic time step.

To validate the flow computation, wall pressure fluctuations were measured with 6 differential miniature pressure transducers XCS-093-1psi D (Kulite Semiconductor Products) with a diameter of 2.5 mm (see Fig. 7b). The sensors were flush mounted and equally spaced along a line on the duct. Exemplary, the spectral density (PSD) of the instationary pressure in Fig. 10 at position K2 and K4 is displayed (for

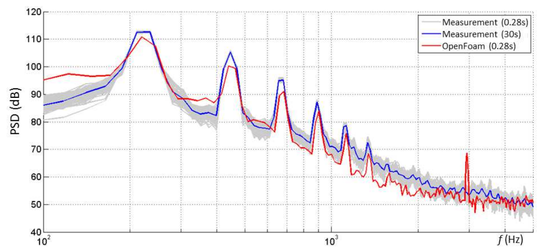

(a) Position 2

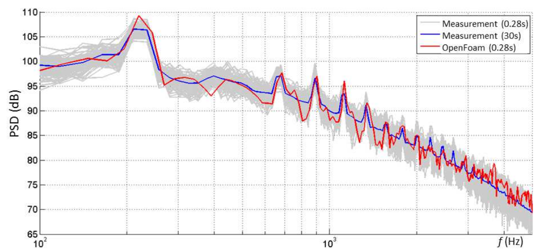

(b) Position 4

Figure 10. Spectral density (relative to 20μPa) of the measured instationary pressures at position K2 and K4.

positions see Fig. 7b). Here, it should be emphasized that especially a good comparison between measured and simulated pressure spectra is of high relevance since the instationary pressure is a key physical quantity within aeroacoustic computations.

In accordance to the flow computation, the rotating domain is embedded into a quiescent propagation region for performing the acoustic simulations (see Fig. 11) [27]. Furthermore, at the inflow and outflow boundaries of the CFD domain two additional regions as PML are added to effectively approximate acoustic free field conditions [40]. To resolve

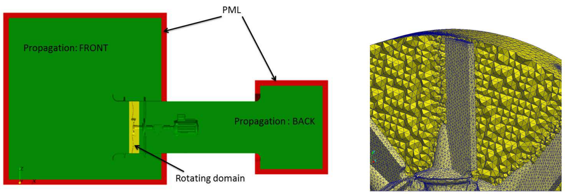

(a) Computational setup **(b) Detail of mesh**

Figure 11. Computational domain for the acoustic calculation and detail of acoustic mesh near the rotor.

accurately the rotor geometry, tetrahedron elements are used as displayed in Fig. 11b. As soon as the inlet as well as the outlet are reached, hexahedron elements are used and the two meshes are coupled by a Nitsche-type mortaring approach. The computational mesh resulted in approximately 2 million cells, which is by a factor of 15 smaller than the flow grid. Thereby, the spatial resolution of the mesh has been chosen to resolve acoustic waves up to 5 kHz (about ten finite elements with linear basis functions per wavelength), which was the main frequency range of interest. The used time-stepping scheme with controlled dispersion (Hilber-Hughes-Taylor) numerically damps waves of higher frequency to avoid numerical artifacts. Therefore, the computed acoustic spectra will strongly decrease above 5 kHz (see Figs. 12a and 12b). The mesh convergence has been studied by placing artificial sources on the rotor blades. The computation of the acoustic sources on the flow grid are interpolated to the acoustic grid via a cut-volume-cell approach [42, 43].

The sound field was measured with four 1/2 inch free-field microphones, type 4189-L-001 (Brüel & Kjaer) arranged in a quarter-circle with a radius of 1 m around the inlet bellmouth in a horizontal plane at the same height as the rotational axis, see Fig. 8b. Thereby, the measurements were made synchronized with the wall pressure fluctuations. Accordingly, measurement time was 30 s with a sampling frequency of 48 kHz. Figures 12 display the computed power spectral density of the acoustic pressure at the two microphone positions (for location see Fig. 8b). Thereby, the smoothed measured spectra obtained from the 30 s recorded acoustic pressure signals as well as the individual spectra by just using measured data of 0.1 s (in gray) are displayed. The computed spectra based on the numerical simulations using openCFS [44] are calculated out of a real-time simulation of 0.06 s. Further details on the numerical

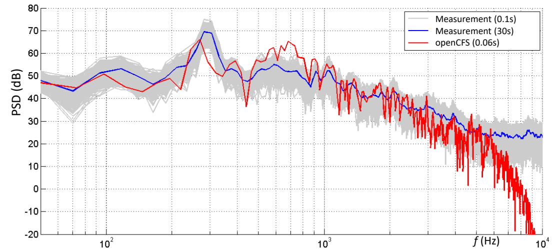

(a) Position M1

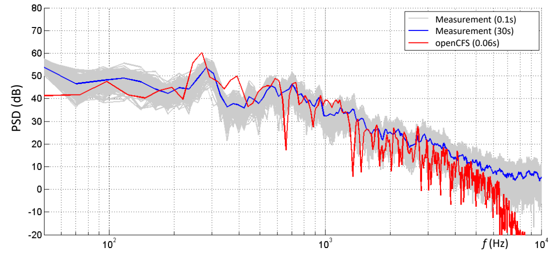

(b) Position M4

Figure 12. Spectral density (relative to 20μPa) of the measured microphone signals at position M1 and M4.

computations can be found in [42].

3.3. Cavity with a lip

This benchmark case by [45] considers a flow - acoustic feedback mechanism. The geometrical properties are given in Fig. 13, with all spatial dimensions in mm. The deep cavity has a reduced

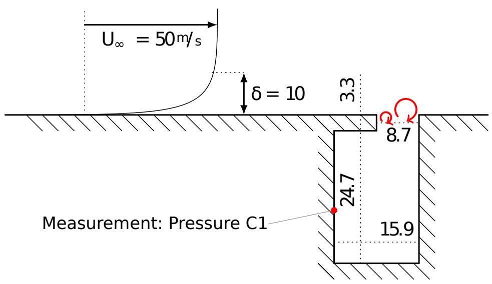

Figure 13. The geometry and the flow configuration of the benchmark problem, cavity with a lip.

cross-section at the orifice and the cavity separates two flat plate configurations. The flow, with a free-stream velocity of $U_\infty = 50$ m/s, develops over the plate up to a boundary layer thickness of $\delta = 10$ mm. For this configuration the first shear layer mode is expected at about $f_{s1} = 1.7$ kHz.

The unsteady, compressible, and laminar flow simulation is performed with a prescribed velocity profile $\underline{u} = \underline{u}_{in}$ at the inlet Γ_1, a no slip and no penetration condition $\underline{u} = \underline{0}$ for the wall Γ_2, an enforced reference pressure $p = p_{\mathrm{ref}}$ at the outlet Γ_3, and a symmetry condition $\underline{u} \cdot \underline{n} = 0$ at the top Γ_4 (see Fig. 2). Thereby, the commercial CFD software Ansys-Fluent has been used. The compressible flow simulation demonstrates the presence of standing waves due to the boundary conditions of the compressible flow simulation as displayed in Fig. 14. This shows

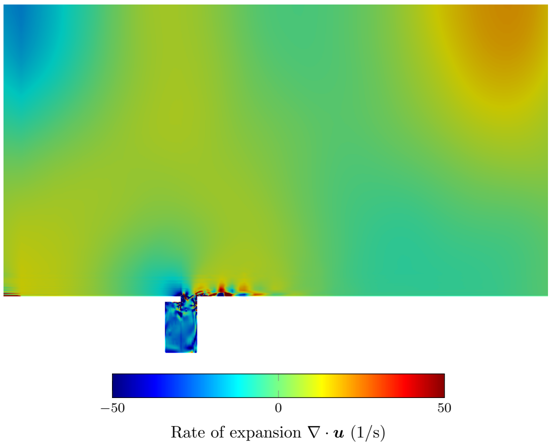

Figure 14. The rate of expansion $\nabla \cdot \underline{u}$ of the compressible flow simulation at a representative time step.

how important it is to model boundaries with respect to the physical phenomena.

For each time step of the compressible flow computation, Eq. (27) is solved with the appropriate boundary conditions

$$\underline{n} \times \nabla \times \underline{A}^{*,\mathrm{ic}} = \underline{n} \times \underline{u} \ \text{ on } \ \Gamma_{1,2,3,4}$$

to obtain the pure vortical velocity field according to Eq. (29) (see Fig. 15). This method tackles the

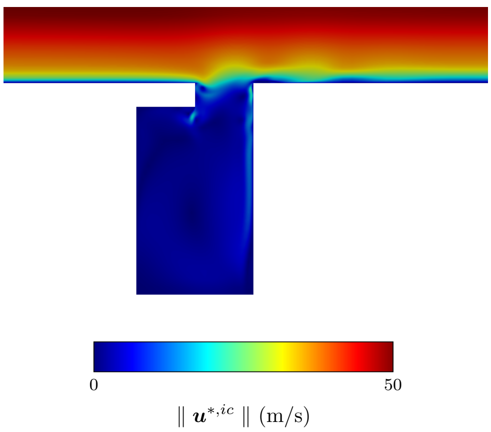

Figure 15. The magnitude of the incompressible component of the flow velocity captures the vortical flow features of the simulation.

compressible phenomena inside the domain Ω_{F} by filtering the domain artifacts of the compressible flow field such that the computed sources are not corrupted. Figure 16 illustrates the shape and nature of the Lamb vector (Fourier-transformed) at the first shear layer mode, where the difference between the corrected and non-corrected Lamb vector gets visible.

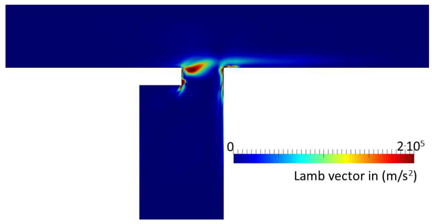

(a) $x-$ **component of Lamb vector**

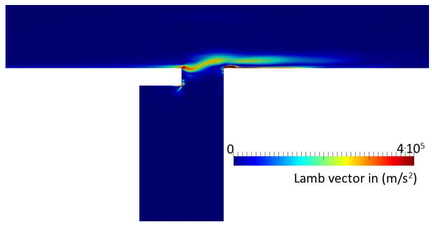

(b) $y-$ **component of Lamb vector**

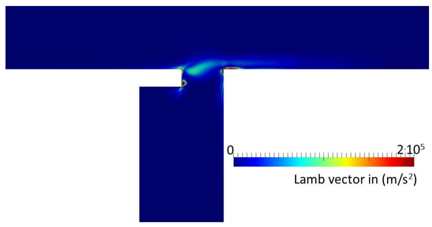

(c) $x-$ **component of corrected Lamb vector**

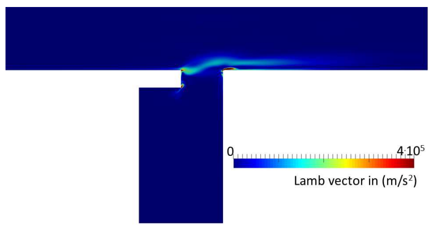

(d) $y-$ **component of corrected Lamb vector**

Figure 16. Comparison of the Lamb vector for the corrected and the non-corrected calculation at the first shear layer mode.

The acoustic simulations utilizes the equation of vortex sound Eq. (31) to compute the acoustic propagation applying the finite element method by using the in-house solver openCFS [44]. Two different aeroacoustic source variants are investigated, the uncorrected Lamb vector $\underline{L}(\underline{u})$ (field quantities directly from the compressible flow simulation) and the corrected Lamb vector $\underline{L}(\underline{\tilde{u}})$ based on the Helmholtz decomposition in the vector potential formulation. Figure 17 compares the resulting acoustic fields. As expected, the acoustic field computed by the corrected source term is strongly reduced in amplitude and shows a typically wave propagation, whereas Fig. 17a shows perturbations.

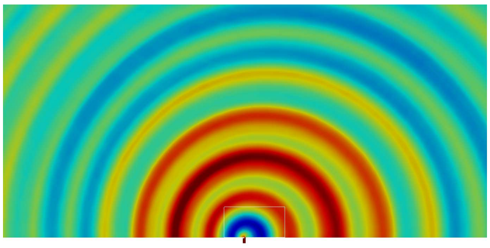

(a) $\underline{L}(\underline{u}) = \underline{\omega} \times \underline{u}$**, not corrected**

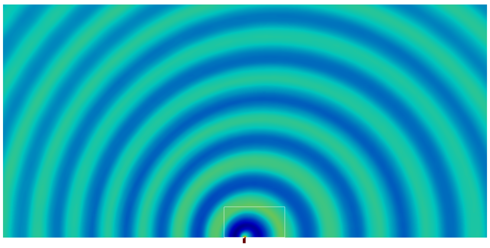

(b) $\underline{L}(\underline{\tilde{u}}) = \underline{\omega} \times \underline{\tilde{u}}$**, corrected**

Figure 17. Field of the total enthalpy fluctuation *H* at a characteristic time.

The ideal gas law and Eq. (30) serves us a relation between the specific enthalpy H and the sound pressure p^{a}. In its linearized form, the sound pressure level (SPL) computes by

$$SPL = 20 \log \left(\frac{\rho_0 H}{p_{\mathrm{a,ref}}} \right) \tag{38}$$

with $p^{\mathrm{a}}_{\mathrm{ref}}$ being $20\,\mu$Pa. Table 1 quantifies the obtained results for the first shear layer mode in the far field, where the computed 2D acoustic sound pressure has been scaled according to [46] for comparison with the measured data. Thereby, the computations of the non-corrected source terms overestimate the experimental result by 22 dB. In the case of the corrected source terms, the overestimation is just 4 dB.

Table 1. Comparison of the pressure outside the cavity

	$f_{\mathrm{s1}}/\mathrm{Hz}$	$SPL_{\mathrm{s1}}/\mathrm{dB}$
Experiment	1650	30
Simulation $\underline{L}(\underline{\tilde{u}}) = \underline{\omega} \times \underline{\tilde{u}}$	1660	34
Simulation $\underline{L}(\underline{u}) = \underline{\omega} \times \underline{u}$	1660	52

4. SUMMARY

This article has discussed physical models and numerical schemes for computational aeroacoustics. In doing so, the main challenges for flow induced sound both for low and high Mach number flows have been highlighted. The discussed physical models concentrate on aeroacoustic analogies and perturbation equations based on systematic decomposition of physical field properties. Although main achievements have been obtained within the last twenty years, aeroacoustics is still a topic of ongoing research with many phenomena, which are partially not fully understood or / and needs physical models and numerical computational schemes to support their understanding.

ACKNOWLEDGEMENTS

The authors acknowledge support from the Austria Research Promotion Agency (FFG) under no. 867971 and no. 874784.

REFERENCES

[1] Hardin, J. C., and Hussaini, M. Y. (eds.), 1992, *Computational Aeroacoustics*, chap. Computational aeroacoustics for low Mach number flows, Springer-Verlag, pp. 50–68, new York.

[2] Hardin, J. C., and Hussaini, M. Y. (eds.), 1992, *Computational Aeroacoustics*, chap. Regarding numerical considerations for computational aeroacoustics, Springer-Verlag, pp. 216–228, new York.

[3] Wagner, C., Hüttl, T., and Sagaut, P. (eds.), 2007, *Large-Eddy Simulation for Acoustics*, Cambridge University Press.

[4] Schoder, S., and Kaltenbacher, M., 2019, "Hybrid Aeroacoustic Computations: State of Art and New Achievements", *Journal of Theoretical and Computational Acoustics*, Vol. 27 (04), p. 1950020.

[5] Bailly, C., Bogey, C., and Marsden, O., 2010, "Progress in direct noise computation", *International Journal of Aeroacoustics*, Vol. 9 (1-2), pp. 123–143.

[6] Frank, H., and Munz, C. D., 2016, "Direct aeroacoustic simulation of acoustic feedback phenomena on a side-view mirror", *Journal of Sound and Vibration*, Vol. 371, pp. 132–149.

[7] Fares, E., Duda, B., and Khorrami, M. R., 2016, "Airframe Noise Prediction of a Full Aircraft in Model and Full Scale Using a Lattice Boltzmann Approach", *22nd AIAA/CEAS Aeroacoustics Conference*, p. 2707.

[8] Sanders, L., Manoha, E., Murayama, M., Yokokawa, Y., Yamamoto, K., and Hirai, T., 2016, "Lattice-Boltzmann Flow Simulation of a Two-Wheel Landing Gear", *22nd AIAA/CEAS Aeroacoustics Conference*, p. 2767.

[9] Lighthill, M., 1952, "On sound generated aerodynamically I. General theory", *Proc Roy Soc Lond*, (A 211), pp. 564–587.

[10] Crighton, D. G., Dowling, A. P., Ffowcs-Williams, J. E., Heckl, M., and Leppington,

F. G., 1992, *Modern methods in analytical acoustics*, Springer Lecture Notes.

[11] Phillips, O. M., 1960, “On the generation of sound by supersonic turbulent shear layers”, *J Fluid Mech*, Vol. 9, pp. 1–18.

[12] Lilley, G. M., 1974, “On the noise from jets”, *Tech. rep.*, AGARD CP-131.

[13] Goldstein, M. E., 1976., *Aeroacoustics*, McGraw-Hill.

[14] Curle, N., 1955, “The Influence of Solid Boundaries upon Aerodynamic Sound”, *Proceedings of the Royal Society of London A: Mathematical, Physical and Engineering Sciences*, Vol. 231 (1187), pp. 505–514.

[15] Williams, J. E. F., and Hawkings, D. L., 1969, “Sound Generation by turbulence and surface in arbitratry motion”, *Philosophical Transactions of the Royal Society of London, Series A, Mathematical and Physical Sciences*, Vol. 264, pp. 321–342.

[16] Morgan, W. R., 1930, “The Kirchhoff Formula Extended to a Moving Surface”, *Philosophical Magazine*, Vol. 9, pp. 141–161.

[17] Prieur, J., , and Rahier, G., 2001, “Aeroacoustic integral methods, formulation and efficient numerical implementation”, *Aerospace Science and Technology*, Vol. 5 (7), pp. 457–468.

[18] Astley, R. J., Sugimoto, R., Achunche, I. M., Kewin, M. F., Mustafi, P., and Deane, E. P., 2010, “Reprint of: A review of CAA for fan duct propagation and radiation, with application to liner optimisation”, *Procedia IUTAM*, Vol. 1, pp. 143–152.

[19] Crow, S. C., 1970, “Aerodynamic sound emission as a singular perturbation problem”, *Studies of Applied Mathematics*, Vol. 49, pp. 21–44.

[20] Hardin, J. C., and Pope, D. S., 1994, “An acoustic/viscous splitting technique for computational aeroacoustics”, *heoretical and Computational Fluid Dynamics*, pp. 323–340.

[21] Shen, W. Z. and Sørensen, J. N., 1999, “Aeroacoustic Modelling of Low-Speed Flows”, *Theoretical and Computational Fluid Dynamics*, Vol. 13, pp. 271–289.

[22] Ewert, R., and Schröder, W., 2003, “Acoustic perturbation equations based on flow decomposition via source filtering”, *Journal of Computational Physics*, Vol. 188, pp. 365–398.

[23] Seo, J., and Moon, Y., 2005, “Perturbed Compressible Equations for Aeroacoustic Noise Prediction at Low Mach Numbers”, *AIAA Journal*, Vol. 43, pp. 1716–1724.

[24] Munz, C., Dumbser, M., and Roller, S., 2007, “Linearized acoustic perturbation equations for low Mach number flow with variable density and temperature”, *Journal of Computational Physics*, Vol. 224, pp. 352 – 364.

[25] Hüppe, A., 2013, “Spectral Finite Elements for Acoustic Field Computation”, Ph.D. thesis, University of Klagenfurt, Austria.

[26] Hüppe, A., Grabinger, J., Kaltenbacher, M., Reppenhagen, A., and Kühnel, W., 2014, “A non-conforming finite element method for computational aeroacoustics in rotating systems”, *American Institute of Aeronautics and Astronautics Conference 2014*.

[27] Kaltenbacher, M., Hüppe, A., Reppenhagen, A., Zenger, F., and Becker, S., 2017, “Computational aeroacoustics for rotating systems with application to an axial fan”, *AIAA journal*, pp. 3831–3838.

[28] Ribner, H. S., 1962, “Aerodynamic Sound from Fluid Dilatations - A Theory of the Sound from Jets and Other Flows”, *Tech. rep.*, Institute for Aerospace Studies, University of Toronto.

[29] Schoder, S., Roppert, K., and Kaltenbacher, M., 2020, “elmholtz’s decomposition for compressible flows and its application to computational aeroacoustics”, *SN Partial Differ Equ Appl*, Vol. 1 (46), pp. 1–20.

[30] Goldstein, M. E., 2003, “A generalized acoustic analogy”, *Journal of Fluid Mechanics*, Vol. 488, pp. 315–333.

[31] Schoder, S., Roppert, K., and Kaltenbacher, M., 2020, “Postprocessing of Direct Aeroacoustic Simulations Using Helmholtz Decomposition”, *AIAA Journal*, Vol. 58 (7), pp. 3019–3027.

[32] Kaltenbacher, M., 2015, *Numerical Simulation of Mechatronic Sensors and Actuators*, Springer, Berlin, 3rd edn.

[33] Howe, M. S., 2003, *Theory of Vortex Sound*, Cambridge Texts in Applied Mathematics.

[34] Lee, D. J., and Koo, S. O., 1995, “Numerical study of sound generation due to a spinning vortex pair”, *AIAA Journal*, Vol. 33 (1), pp. 20–26.

[35] Slimon, S. A., Soteriou, M. C., and Davis, D. W., 1999, “Computational aeroacoustics simulations using the expansion about incompressible flow approach”, *AIAA journal*, Vol. 37 (4), pp. 409–416.

[36] Hardin, J. C., and Pope, D. S., 1994, “An acoustic/viscous splitting technique for computational aeroacoustics”, *Theoretical and Computational Fluid Dynamics*, Vol. 6 (5), pp. 323–340.

[37] Müller, E. A., and Obermeier, F., 1967, “The spinning vortices as a source of sound”, *AGARD CP-22*, pp. 22–1.

[38] Schoder, S., Roppert, K., Weitz, M., Junger, C., and Kaltenbacher, M., 2020, “Aeroacoustic source term computation based on radial basis functions”, *International Journal for Numerical Methods in Engineering*, Vol. 121 (9), pp. 2051–2067.

[39] Kaltenbacher, M., 2018, *Computational Acoustics*, CISM International Centre for Mechanical Sciences, Springer International Publishing, ISBN 9783319590387.

[40] Kaltenbacher, B., Kaltenbacher, M., and Sim, I., 2013, “A modified and stable version of a perfectly matched layer technique for the 3-d second order wave equation in time domain with an application to aeroacoustics.”, *Journal of Computational Physics*, Vol. 235, pp. 407–422.

[41] Zenger, F., Junger, C., Kaltenbacher, M., and Becker, S., 2016, “A Benchmark Case for Aerodynamics and Aeroacoustics of a Low Pressure Axial Fan”, *SAE Technical Paper*, SAE International.

[42] Schoder, Stefan, Junger, Clemens, and Kaltenbacher, Manfred, 2020, “Computational aeroacoustics of the EAA benchmark case of an axial fan”, *Acta Acustica*, Vol. 4 (5), p. 22.

[43] Schoder, S., Wurzinger, A., Junger, C., Weitz, M., Freidhager, C., Roppert, K., and Kaltenbacher, M., 2021, “Application Limits of Conservative Source Interpolation Methods Using a Low Mach Number Hybrid Aeroacoustic Workflow”, *Journal of Theoretical and Computational Acoustics*, Vol. 29 (01), p. 2050032.

[44] Kaltenbacher, M., 2022, “openCFS - Finite Element solver for Multiphyics”, `http://www.opencfs.org`.

[45] Henderson, B., 2000, “Automobile Noise Involving Feedback- Sound Generation by Low Speed Cavity Flows”, *Tech. rep.*, In: Third Computational Aeroacoustic(CAA) Workshop on Benchmark Problems.

[46] Oberai, A., Roknaldin, F., and Hughes, T. J. R., 2002, “Computation of trailing-edge noise due to turbulent flow over an airfoil”, *AIAA*, Vol. 40 (11).